PROGRAMMABLE MULTIFUNCTIONAL SOFT ORIGAMI ROBOTS

Programmable and reprocessable multifunctional elastomeric sheets for soft origami robots

Shuo Zhang, Xingxing Ke, Qin Jiang, Han Ding*, Zhigang Wu*

Tunable, soft, and multifunctional robots are contributing to developments in medical and rehabilitative robotics, human-machine interaction, and intelligent home technology. A key aspect of soft robot fabrication is the ability to use flexible and efficient schemes to enable the seamless and simultaneous integration of configurable structures. Here, we report a strategy for programming design features and functions in elastomeric surfaces. We selectively modified these elastomeric surfaces via laser scanning and then penetrated them with an active particle–infused solvent to enable controllable deformation, folding, and functionality integration. The functionality of the elastomers can be erased by a solvent retreatment and reprocessed by repeating the active particle infusion process. We established a platform technique for fabricating programmable and reprocessable elastomeric sheets by varying detailed morphology patterns and active particles. We used this technique to produce functional soft ferromagnetic origami robots with seamlessly integrated structures and various active functions, such as robots that mimic flowers with petals bent at different angles and with different curvatures, low-friction swimming robots, multimode locomotion carriers with gradient-stiffness claws for protecting and delivering objects, and frog-like robots with adaptive switchable coloration that responds to external thermal and optical stimuli.

INTRODUCTION

Mimicking bacteria, plants, animals, and even human beings has been a target in robot design, fabrication, and control (*1*, *2*). Living creatures are endowed with iterative feedback mechanisms that empower sensitive perceptibility, sophisticated and agile mobility, and great environmental adaptability (*3*). Soft robots, made from materials with similar properties, have demonstrated great physical adaptability in many high-profile applications, including human-machine interfaces (*4*), bio-inspired robotics (*5*–*7*), medical operations (*8*–*10*), and exploration (*11*). However, current soft robots, compared with their rigid counterparts, often exhibit less dexterity and precision and poorer autonomous performance. These differences are attributable to insufficient feedback mechanisms and a lack of programmable structures capable of different responses. It is important to develop suitable fabrication schemes that can seamlessly integrate more active materials or heterogeneous structures that can respond to various external stimuli to achieve more powerful performance and advanced functions in the context of soft robots (*12*). By integrating various functional modules into intrinsically programmable smart materials/structures, a number of advanced soft robots have been developed recently. These include entirely soft, autonomous robots embedded with logical microfluidic actuator systems (*13*), an ultrathin electronically innervated crawling robot for sensing external light and heat (*14*), a biosensing soft robot for autonomously parsing chemical signals via integrated organic and inorganic interfaces (*15*), and a small-scale soft robot with multimodal locomotion (*16*).

In addition to traditional fabrication and assembly techniques, a number of approaches have been developed for seamless integration of functional/heterogeneous materials into intrinsically soft programmable structures (*2*). The capability to introduce a hierarchy of many materials using three-/four-dimensional (3D/4D) printing technology shows great potential for enabling digital fabrication of various heterogeneous structures into soft robots with diverse and interesting mechanical, electrical/electronic, optical, magnetic, thermal, chemical, and biological features (*17*–*21*). Such rich multifunctionality can substantially enhance the robots' capabilities, mobility, dexterity, and other features, radically changing the current approaches to design, control, and fabrication for soft robots (*1*). For example, Wood and colleagues (*22*) used a 3D-printed graded structure to make an untethered soft robot exhibit agile movement, and Zhao and colleagues (*23*) demonstrated rapid transformations in various magnetic soft robots achieved by embedding heterogeneous magnetic domains into 3D-printed soft materials. However, as a platform technology, multimaterial 3D/4D printing to produce soft robots is still not well developed for many specific fields and applications. These techniques often require an integrated design and fabrication strategy (*13*), elongating the learning curve for beginners.

Other alternatives have also been developed. One of the most convenient techniques is skin technology (*24*–*28*). Simply laminating or conformably printing (*29*) functional layers onto soft robots helps achieve perception and has been conducted to produce a robot with highly sensitive tactile detection (*30*) and actively perceiving and responsive soft robots with sensitive triboelectric energy-harvesting skins (*31*). This is an efficient way to integrate functional modules into a soft robot without considering the detailed internal structure and function of the robot body, thereby substantially decreasing the complexity of design and fabrication (*32*, *33*). However, there is potential for delamination to occur as result of stress mismatch under harsh and dynamic conditions. Conformal integration on 3D surfaces is still challenging and is not currently widely applicable for soft robots (*34*, *35*).

Derived from self-assembly, origami is regarded as a simple fabrication technology to decouple design from fabrication complexity when making multifunctional robots (*36*–*38*), including the flying microrobots from Wood's group (*39*, *40*). Traditionally, as one of the tools for implementing origami techniques, selective swelling-led asymmetrical expansion has proven to be a useful general technique for achieving 3D geometric programmability (*41*). However,

State Key Laboratory of Digital Manufacturing Equipment and Technology, School of Mechanical Science and Engineering, Huazhong University of Science and Technology, Wuhan 430074, China.
*Corresponding author. Email: zgwu@hust.edu.cn (Z.W.); dinghan@hust.edu.cn (H.D.)

to be a bulk technology, a comprehensive consideration of design and fabrication is necessary when implementing such an approach. It is often difficult to reprocess both the geometry and functional modules, and few studies on adaptive locomotion modes or responses to external stimuli have been conducted. Thus, it is worthwhile to develop facile fabrication schemes that seamlessly integrate diverse actuating and sensing modules into soft programmable and even reprocessable structures to achieve multifunctionality.

Here, we developed a facile technique for rapidly fabricating soft ferromagnetic 3D origami robots with programmable and reprocessable structures, actuation, and functions (Fig. 1) from 2D elastomeric sheets by combining selective tuning surface morphology using an ultraviolet (UV) laser and penetrating them with an active particle–infused solvent. We present several shape-programmable origami robots, such as soft robots that mimic flowers with petals bent at different angles and with different curvatures; multifunction-configurable robots, such as a low-friction swimming robot with both actuating and superhydrophobic surfaces and butterfly-like robots with UV-luminescence sensing and ferromagnetic actuation capabilities; an adaptive multimode locomotion carrier with stiffness-gradient claws for protecting and delivering objects; and a frog-like robot with adaptive and switchable coloration that responds to external thermal and optical stimuli. Our fabrication scheme provides a platform for producing soft robots with programmable and reprocessable shapes, actuation, and sensing. This scheme offers a rapid, flexible tool for seamlessly integrating multiple materials simultaneously into soft robots, thereby laying a solid foundation for the development of higher-functioning/intelligence robots.

RESULTS

Preparation of programmable and reprocessable multifunctional elastomeric sheets

We used a cost-efficient UV laser to selectively scan and pattern the surface of a 2D elastomeric sheet made of carbon-doped polydimethylsiloxane (cPDMS) (Fig. 1A). During our initial investigations (shown in text S1 and fig. S1), cPDMS exhibits high absorption of 355-nm UV light regardless of its thickness, resulting in a rough surface topography and good deformability. The laser-scanned elastomer sheet exhibits more solvent-philic (38.5°) behavior, whereas the pristine sheet, not exposed to the laser, exhibits relatively more "solvent-phobic" (73.6°) behavior. (We note that compared with the laser-scanned sheet, the behavior of the nonprocessed sheet here is relatively more solvent-phobic, but strictly, it should be defined as solvent-philic instead of solvent-phobic because the contact angle is less than 90°.) This provides a simple way for selectively wetting the surface to make the active particle–infused solvent penetrate into selected regions.

By adjusting the operational parameters of the laser and the thickness of the elastomeric sheet, we can tune the surface topography (roughness) of laser-treated areas to obtain specific anisotropic microgrooves. This leads to a heterogeneous swelling effect (deformation/folding), transforming 2D elastomeric sheets into 3D shapes in a process of programmed origami by active particle–infused solution (e.g., ferrofluid) wetting, absorption, and penetration (Fig. 1B). After being swollen, such programmable 3D shapes can be "memorized" via immobilization of a stiff layer of iron oxide–based nanoparticles on the surface. Such a ferromagnetic particle–doped surface can serve as an effective locomotion/actuation module that can respond to external stimuli as needed. Other functional materials dispersed in a PDMS-compatible solution, e.g., quantum dot (QD) solutions and thermochromic inks, can also be seamlessly integrated into such origami soft robots simultaneously, endowing the soft robot with sensing and other functions, e.g., the ability to respond to external optical and thermal fields based on switchable coloration. Furthermore, after solvent evaporation, the folded 3D shape can be re-swollen in the appropriate solvent, leading to the erasure of the stiff agglomerated layer as a result of forces of expansion and to a return to the original 2D elastomeric state (Fig. 1C). The structural and functional modules can then be reprocessed by repeating the above processes.

Photographs and contact angles of ferrofluid droplets on both pristine and scanned surfaces are shown in the inset

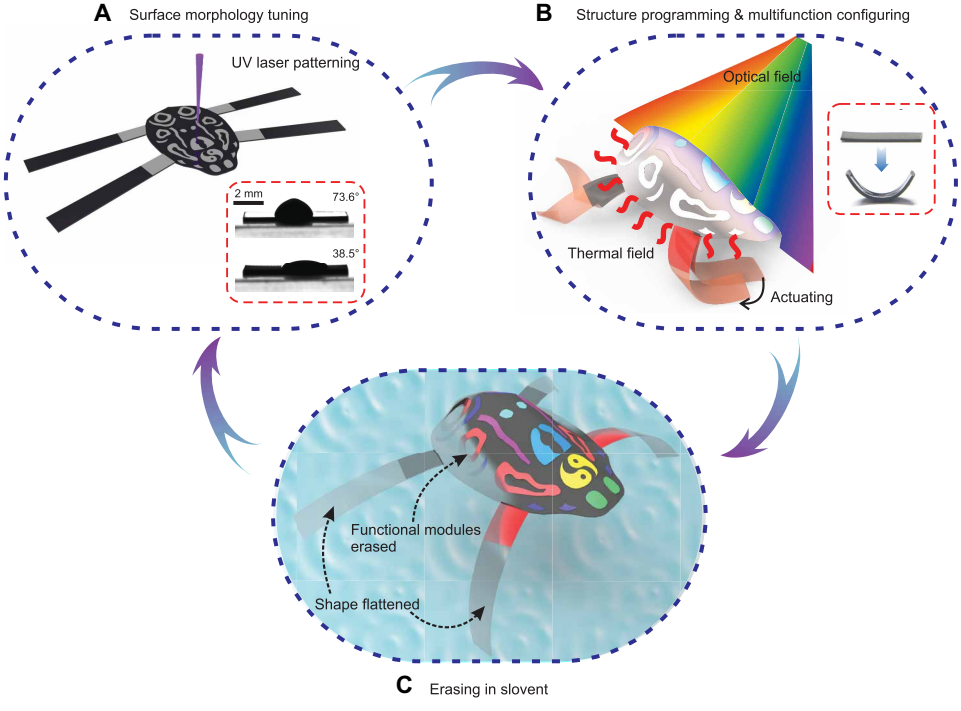

Fig. 1. Schematic illustrations of programmable and reprocessable multifunctional elastomeric sheets for soft origami robots. (**A**) Surface morphology–tuned elastomeric sheet via selective UV laser scanning, showing a more solvent-philic area (the bottom photo of the inset) compared with the pristine surface (the top photo of the inset). (**B**) Structural programming and seamless multimaterial infusing via local active particle agglomeration and subsequent heterogeneous deformation memorization (inset), resulting in magnetic actuation and different coloration responses to optical and thermal stimuli. (**C**) Deformed structures flattened, functional modules erased, and original shape recovered in the solvent.

of Fig. 1A, and field-emission scanning electron microscopy (FSEM) images are shown in fig. S2A. Compared with the pristine surface, the laser-scanned surface is more ferrofluid-philic, with a smaller static contact angle. Such a high wettability difference between the laser-scanned and pristine surfaces facilitates precise placement of ferrofluid droplets at designated locations on the laser-scanned surface, because ferrofluid droplets can roll over a pristine surface but are largely restricted from moving on the laser-scanned surface and are absorbed into the elastomeric matrix (text S2 and fig. S3). Furthermore, the separation of laser-treated structures offers more areas for deforming of heterogeneous swollen regions (compare, for example, the geometry and deformation of the samples in fig. S2, B to D). The residual iron-based nanoparticles are agglomerated on the surface after solvent evaporation and generate a continuous stiff layer that provides mechanical strength and can also serve as an actuating module.

Selective morphology tuning and elastomeric sheet programming

As revealed in a previous study, PDMS is compatible with many organic solvents (*42*), and it can be considered as a "solid solution" (*43*). When PDMS comes into contact with nonpolar solvents (e.g., hydrocarbons or hydrocarbons dissolved with small molecules), it absorbs them and swells spontaneously. To better understand selective morphology tuning and subsequent heterogeneous solvent treatment–induced origami, we conducted a series of experiments using a ferrofluid (iron oxide colloid) and diesel colorant–mixed ferrofluid (hereinafter referred to as colored ferrofluid) to visualize the whole process. As shown in Fig. 2A (illustrations and experimental photos), fig. S4, and movies S1 and S2, the process can be divided into four critical sequential stages:

1) Selective solvent wetting. After the ferrofluid and colored ferrofluid droplets are dripped onto the laser-scanned surface of cPDMS and cPDMS-PDMS composite, respectively, the solvent carrier (a mixture of hydrocarbons from *n*-decane to tetradecane) is absorbed and penetrates into the silicone rubber matrix.

2) Penetration of solvent into elastomeric surface layer and resultant deformation. Because of the high intermiscibility of the hydrocarbon solvent and elastomeric sheet, the solvent rapidly diffuses along its concentration gradient from the surface layer to the inner layers. Consequently, the upper part of the elastomeric sheet becomes swollen and expands. Simultaneously, most of the dispersed nanoscale iron oxide particles concentrate and precipitate out, and some of them adhere to the treated surface because of the rapid loss of solvent. The elastomeric sheet is observed to hunch up during this stage. As the cPDMS-PDMS sample in fig. S4B shows, the surface layer turns blue because the colored solvent diffuses and penetrates into the PDMS matrix from the top layer downward (images were obtained at 3 and 6 min).

3) Penetration of solvent into the bulk of the elastomeric sheet and resultant deformation. As the solvent continues to diffuse and penetrate into the bulk of the elastomeric layer, the lower layers of the elastomeric sheet begin to swell and expand, while swelling of the upper layers diminishes because of solvent evaporation, resulting in a concave shape that is the opposite of the shape that develops in the second step. During this third stage, iron oxide nanoparticles continue to clump on the surface as a result of solvent evaporation. Similarly, the blue area in the cPDMS-PDMS composite expands into the bulk of the PDMS, with the colored solvent continuing to diffuse and penetrate (images in fig. S4B were obtained at 7, 10, and 12 min).

4) Deformation memorization. After the above steps, the solvent diffuses into the bottom layer of the elastomer (the blue area diffuses throughout the silicone matrix, as shown in the images obtained at 22 min in fig. S4B), resulting in the largest deformation. The iron oxide nanoparticles become agglomerated on the scanned surface, producing a continuous stiff layer. The 3D shape is thereby immobilized and does not notably change afterward, allowing it to play an important role in the memorization of the deformed 3D shape. As a control, we conducted a similar configuration process with the pure solvent carrier. The sample also swelled and deformed but eventually reverted to its original 2D state because of the absence of agglomerated iron-based particles (fig. S5). As the complementary FSEM and electro-probe x-ray microanalyzer (EPMA) images in Fig. 2B and fig. S6 show, most of the iron oxide nanoparticles are enriched on the surface and form a continuous stiff layer, while a few of them are found in the superficial layer close to the surface.

To further study the dependence of the programmable swelling and deforming processes on the laser's operational parameters, we measured the bending angles (θ), twisting angles (β), and curvatures (ρ) during the configuration. To rule out the possible influences of the carbon black doped in the PDMS-precured mixture and the volume of ferrofluid, we used cPDMS (a 10-g silicone base and 1-g curing agent mixture with 0.1 g of carbon black) and 2 μl of ferrofluid in all of the relevant measurements (fig. S7). As illustrated in Fig. 2C, by adjusting the orientation of the laser-treated microgrooves (α), the adjacent distance between laser scanning routes (ΔL), and the thickness of the sample (t), we were able to tune the surface morphology (roughness) and thereby control the corresponding 3D shaping characteristics. For twisting, as α increases, both the β and ρ of twisted 3D structures decrease (Fig. 2D); as t increases, ρ decreases; and when ΔL = 0.05 or 0.1 mm, ρ is maximized (fig. S8). Thus, the twistability, twisting angle, and curvature of the structure are related to the orientation of the microgrooves, the sample thickness, and the adjacent distance between scanning routes, respectively. For bending, as ΔL changes from 0.005 to 0.2 mm, the surface roughness (*Sa*) peaks at ~24.5 μm when ΔL = 0.1 mm and then decreases as ΔL increases further (Fig. 2E). The bending angle (θ) and curvature (ρ) exhibit similar trends, peaking at ~219.6° and ~0.6 mm^{-1}, respectively, before decreasing (Fig. 2E). In addition to ΔL, the bendability of the elastomer also depends on its thickness (t): The thinner the elastomer is, the smaller the bending stiffness is. The bending angle (θ) decreases from ~235.4° to ~37.4°, and the curvature (ρ) decreases from ~0.7 to 0.17 mm^{-1} as t increases from 100 to 1000 μm (Fig. 2F) (more details of the deformation process are provided in fig. S9, A and B).

The solvent penetrates and diffuses to the bottom of the bulk of thinner samples faster than that of thicker samples, meaning that it takes shorter amounts of time to go from stage 1 to stage 2 (T_1) and from stage 3 to stage 4 (T_2), as shown in Fig. 2G and movie S1. The fastest response time in our tests was less than 3 min, indicating that this fabrication scheme is suitable for use in rapidly configuring soft origami robots. In addition, under our test conditions, lower scanning speeds produce greater surface roughnesses and bending angles, but these characteristics are independent of the pulse repetition frequency of the laser (fig. S9C).

Theoretically, we can program and configure numerous 3D shapes by bending and twisting of specific structures. As shown in Fig. 2H, a simple deformation obtained by bending and twisting of different structures will lead to totally different 3D shapes. These include, for example, cyclic serpentine strips, twice-twisted shuriken-like origami

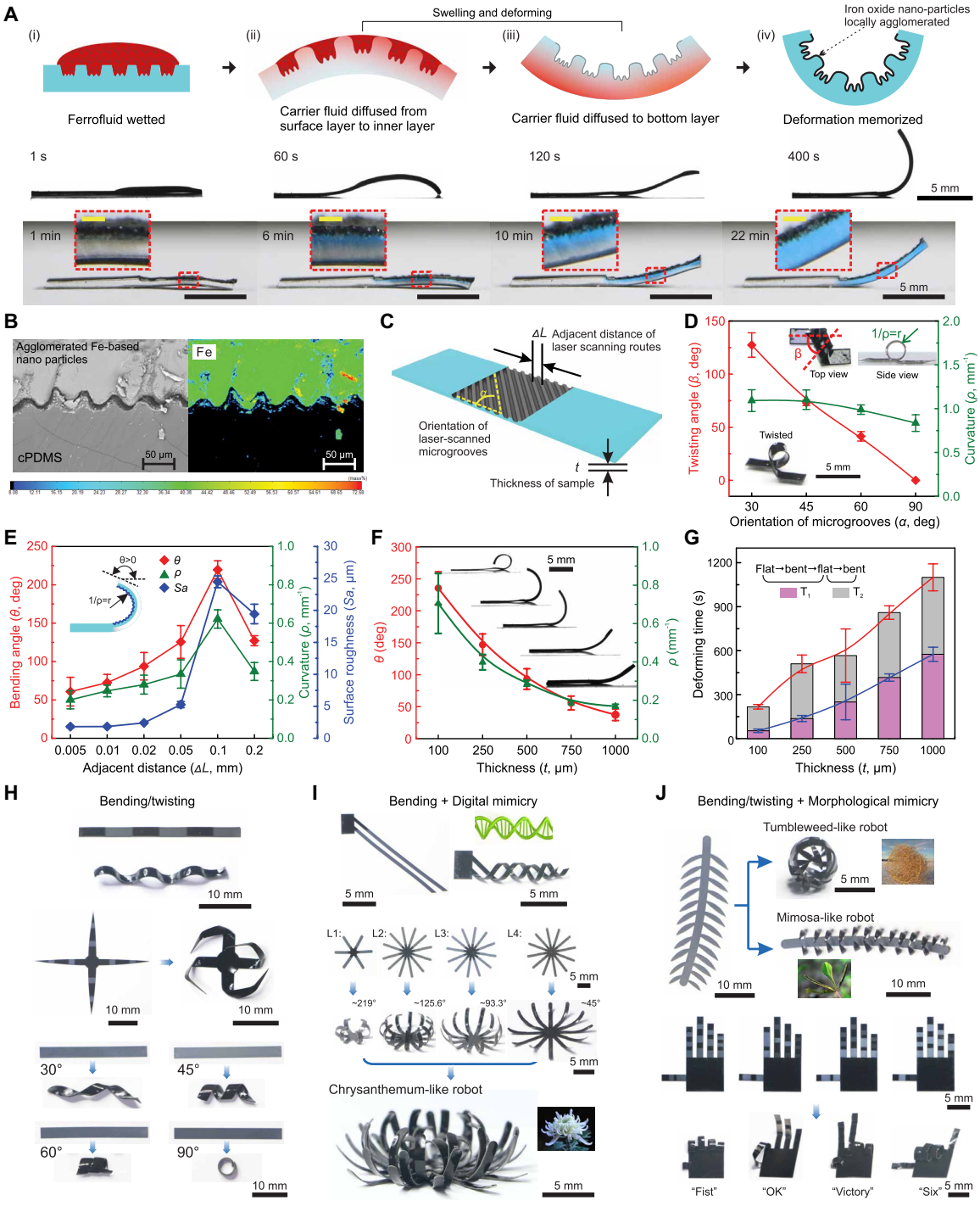

Fig. 2. Mechanism, characterization, and demonstrations of programmable configuration (from 2D elastomeric sheets to 3D origami robots). (**A**) Schematic illustration (first row) of configuration mechanism and process, with corresponding photographs of ferrofluid-penetrated cPDMS (second row) and diesel colorant–mixed ferrofluid penetrated into cPDMS-PDMS composite (third row). Scale bars (insets), 500 μm. Note that for the purpose of observation of an obvious color gradient, the thickness of the composite (~800 μm) was greater than that of the cPDMS (~250 μm), so that the diffusion time between them was different. (**B**) FSEM and EPMA images of the cross profile of a configured sample. The rainbow color scale represents the mass content of the element. (**C**) Illustration of the configuration programming by controlling parameters for tuning surface morphology. (**D**) Relationship between the twisting angles, curvature, and orientation of microgrooves in twisting deformation. Insets illustrate the measurement of twisted samples. Points are the average of three trials, and error bars show ±1 SD. (**E** and **F**) Bending angles and curvatures of samples with different adjacent distances (surface roughness) (E) and different thicknesses (F), after shape memorization. (**G**) Deformation times of samples with different thicknesses. (**H** to **J**) Demonstrations of configured soft origami robots based on bending and twisting (H), bending and digital mimicry (I), and bending/twisting and morphological mimicry (J). In (D) to (G), points are average of three trials, and error bars show ±1 SD.

structures, and helix-like origami elastomers with diverse thread pitches. Thus, our strategy suggests a new approach for generating more complex and hybrid origami shapes. Figure 2I shows a double-helix origami structure formed from two parallel intertwined strips and a chrysanthemum-like robot with multilayer elastomeric "petals" with different bending angles and curvatures. The blooming origami flower can be gathered into a closed flower bud using a permanent magnet with a yielding of ~80 mT (fig. S10A). These two demonstrations were accomplished by continuous bending/twisting of coupled predesigned 2D shapes, a process we refer to as digital mimicry. We can also configure biomimetic origami robots in a morphological way. As shown in Fig. 2J, by varying the orientation of the microgrooves on the "stem" part, we can configure the elastomeric leaf as a tumbleweed-like robot or a mimosa-like robot. Similarly, with accurate tuning, an origami hand can be configured to represent different gestures, such as a "fist," an "OK," a "victory," a "six," and many more (fig. S9B), suggesting the potential for development of multifunctional/multimode origami robots. Details of the fabrication parameters for various designs are summarized in fig. S11 and table S1.

Deformation erasure followed structural/functional reprocessing

As found in a previous study, PDMS can absorb some solvents, such as isopropanol (IPA), and this leads to spontaneous swelling and volume expansion (*42*). The memorized 3D shape can be destroyed by stress concentration arising from a mismatch between the expansion ratio of the agglomerated stiff layer and the PDMS substrate. Therefore, the configured structures and the associated functions can be erased by solvent retreatment and then reprocessed by repeating the programming process, as discussed before. To understand the erasure process, we immersed the bent cPDMS and cPDMS-PDMS samples that were configured as shown in Fig. 2A into an IPA bath. The erasure process can be roughly divided into the following four stages, as illustrated in Fig. 3A (illustrations and experimental photos are shown; the details can be found in fig. S12 and movies S1 and S2):

1) Initial stage with a 3D configuration. Iron oxide nanoparticles agglomerate to form a stiff layer on the surface of the elastomer, which deforms into a bent shape (images obtained at 0 min are shown in Fig. 3A and fig. S12).

2) Partial penetration of solvent and delamination of the rigid layer. After being immersed in IPA, the sample is swollen by solvent penetration into the PDMS matrix (the blue area is starting to fade from the edges in the images obtained from 1 to 15 min shown in fig. S12). Because of the large specific surface area of the microgrooves, the layers closer to the rough surface expand more than the internal layers, leading to curvature of the upper layers. Meanwhile, during the flattening process, in the yielding of the heterogeneous swelling capacity, the stress concentration between the soft elastomer matrix and stiff iron oxide layer becomes greater, leading to delamination of rigid iron oxide fragments (fig. S13A).

3) Deep solvent penetration and complete particle detachment. As solvent penetration continues (indicated by the blue area continuing to fade and decrease in images obtained from 20 to 30 min and shown in fig. S12), the iron oxide nanoparticles become mostly detached from the rough surface as the sample continues to swell, deforming into a convex shape.

4) Solvent evaporation and shape recovery. Drying in the ambient environment results in complete solvent evaporation and restoration of the flat surface (the blue area completely fades away, as shown in the images obtained from 30 to 42 min in fig. S12). Images of the elastomers and bending angles during the recovery process are shown in fig. S13 (B and C, respectively). In addition, movie S3 shows several origami robots that have been erased during solvent immersion.

We propose three possible ways to induce new surface morphologies upon the recovery of 2D elastomeric sheets, together with integration of other structural or functional modules (Fig. 3B). "Additive reprocessing" refers to recoating the recovered rough surface with a thin layer of fresh cPDMS and then, after curing, selectively laser repatterning the sample. "Subtractive reprocessing" consists of laser ablating the existing structures to obtain a fully rough surface, followed by selectively rescanning the sample with more powerful laser parameter settings. In this case, the entire laser-scanned surface exhibits a similar ferrofluid-philic character, so that the reprocessing of the ferrofluid-wetted area requires manual deployment to achieve heterogeneous swelling. "Subsurface reprocessing" means repatterning the morphology of the flat surface on the other side of the elastomeric sheet. As shown in Fig. 3C and fig. S14A, the recovered sample was reprocessed into triangular, silk ribbon, and bridge-like shapes. Such robust reconfigurability makes the fabrication scheme more useful and flexible in practical implementation.

To evaluate how many deformation-recovery cycles an elastomeric sheet could undergo, we designed the test shown in fig. S15A. The bending angles and curvatures measured in each of 5 cycles are shown in Fig. 3D, with the maximum θ and ρ being about 160° and 0.50 mm^{-1}, respectively, indicating good repeatability. The complete time courses of both the configuration and erasure are shown in Fig. 3E, with corresponding photographs shown in fig. S15B. Typically, this process can be completed within about 5 min. In addition, the elemental distribution shown in Fig. 3F and fig. S15C reveals that most of the iron oxide–based particles are enriched as a continuous layer on the surface of the elastomer. The shape contrast and repeatability of the three reprocessing methods are shown in fig. S16. Briefly, additive reprocessing enables the greatest number of reuses but is the most difficult to implement because of bonding between the recoated cPDMS layer and the rough surface. Furthermore, the thickness increases as the number of reuses increases, resulting in smaller bending angles. Subtractive reprocessing is the easiest to implement and produces larger bending angles for thinner samples, but the number of times a sample can be reused is smaller than that for additive reprocessing. Subsurface reprocessing enables rapid processing but allows the fewest reuses.

As shown in Fig. 3G and fig. S14B, a flower-like origami robot was reprocessed into fan-like shapes via additive and subtractive reprocessing. Because full scanning reduces the thickness of the recovered sheet in subtractive reprocessing, the transformed shape (on the right) exhibits larger deformation angles than that in additive reprocessing (on the left). Figure 3H and fig. S14C show a hook-like elastomeric ribbon with a magnetic actuation module that was reprocessed with electrical and optical sensing modules by using silver nanowires (AgNWs) and QDs via the "subsurface reprocessing" method. In this demonstration, the electrical sensing provides real-time resistance variation along the direction of motion under a magnetic field; the optical sensing module exhibits a bright emission under UV irradiation. Such a strategy can be further adapted to produce locomotory soft robots. As shown in Fig. 3I and movie S4, a waddling-gait clawing robot can be reprocessed to crawl sideways,

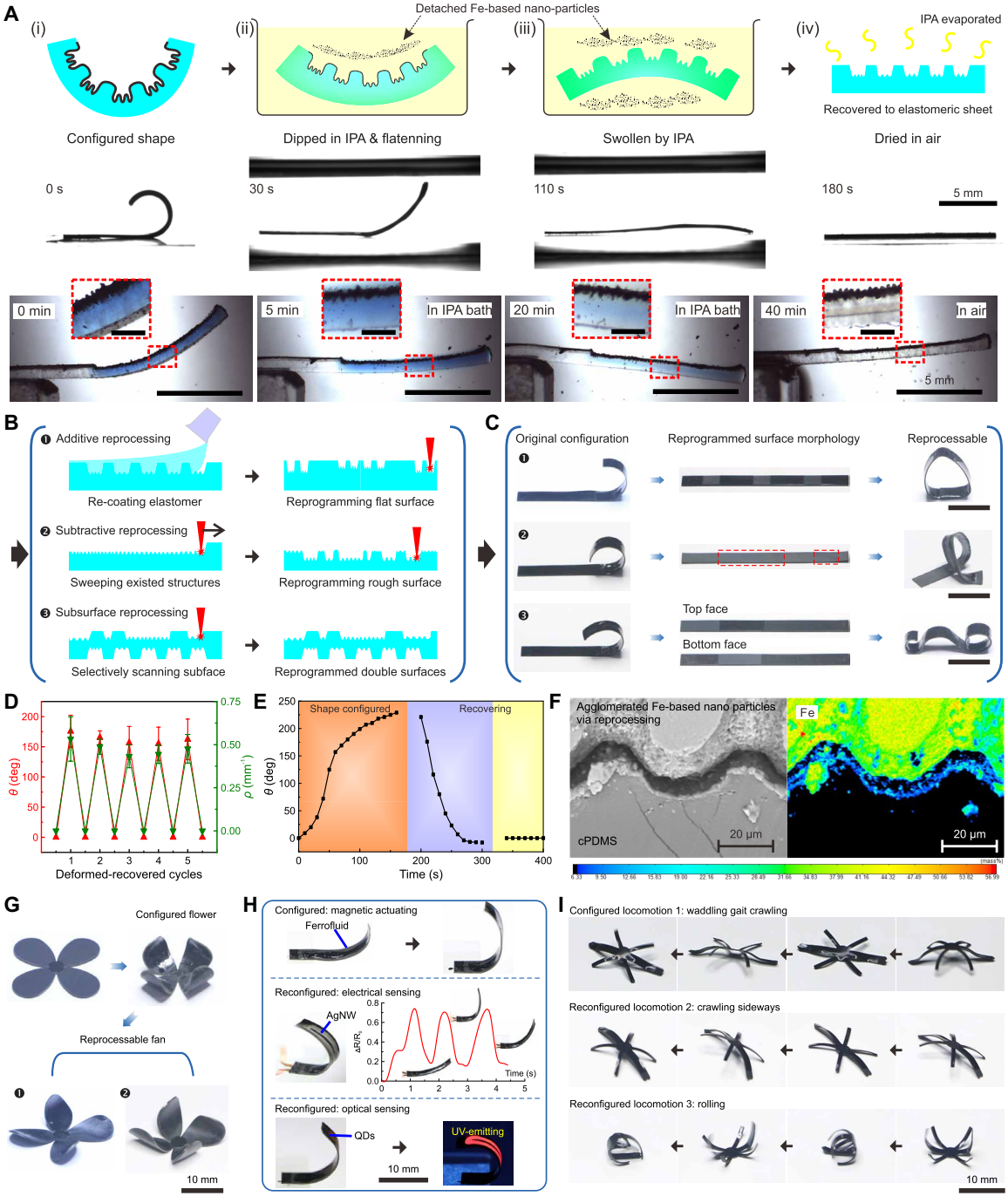

Fig. 3. Mechanism, characterization, and demonstrations of reprocessing (from 3D to 2D and then 2D to 3D). (**A**) Schematic illustration (first row) of recovery mechanism and process in IPA, with corresponding photographs of ferrofluid-penetrated cPDMS (second row) and diesel colorant–mixed ferrofluid penetrated into cPDMS-PDMS composite (third row). Scale bars (insets), 500 μm. Note that for the purpose of observing an obvious color gradient, the thickness of the composite (~800 μm) was larger than that of the cPDMS (~250 μm), so that the diffusion time between them was different. (**B**) Schematic methods for reprocessing the recovered samples: additive, subtractive, and subsurface reprocessing. (**C**) Corresponding photographs of reprocessable origami shapes from a similar hook-like elastomeric ribbon. Scale bars, 10 mm. (**D**) Bending angles and curvatures in a cyclic deformation-recovery test. Points are the average of three trials, and error bars show ±1 SD. (**E**) Bending angles of a cPDMS sample during deformation and recovery. (**F**) FSEM and EPMA images of the vertical profile of a reprocessable sample. The rainbow color scale represents the mass content of the element. (**G** to **I**) Demonstration of structure, sensing, and locomotion modes of reprocessing: (G) deformed origami flower reprocessed into fan-like shapes via additive (left) and subtractive (right) reprocessing methods, respectively; (H) a bent ribbon with a magnetic actuation module reprocessed with electrical sensing and optical sensing modules via the subsurface reprocessing method; (I) waddling-gait crawling origami robot reprocessed into other two locomotion modes: crawling sideways and rolling, via additive and subtractive reprocessing, respectively. The magnitude of magnetic field used for actuation was ~70 mT.

based on varied foot lengths, and to roll (design details are given in fig. S14D). Such a reconfiguration can be transferred to other particle-infused solutions to achieve desired actuations and sensing in soft robots. As shown in fig. S17, when a QD solution ($CsPbBr_3$-hexane) is used, the process of deforming a cPDMS sample was observed to be similar to that of swelling with ferrofluid (fig. S17, A and B), although the relationship between programmable swelling/deforming and laser operational settings, as shown previously in Fig. 2, should be recalibrated according to the new conditions. Nevertheless, because a high-solubility solvent (hexane) (*42*) was used, the deforming and swelling times were much shorter than those achieved with ferrofluid. The particles were mostly agglomerated on the surface, forming a thin layer, according to the SEM images and corresponding elementary analysis (fig. S17, C and D).

Demonstrations of configurable/reprocessable multifunctional soft robots

To incorporate multifunctional surfaces on soft robots, a low-friction surface was integrated onto a magnetic swimming robot to enhance its locomotory performance on a water surface. As shown in Fig. 4A, an elastomeric sheet in the shape of an arrow was selectively treated on each surface using subsurface reprocessing, as described above (fig. S18A). Compared with a pristine elastomer without a 3D configuration, which sank instantly, the 3D laser-treated sheet floated on the surface, as a result of the superhydrophobicity induced by the structured surfaces (Fig. 4A and fig. S18B). The swimming robot was integrated with ferromagnetic actuating modules by selectively treating the upper sides of the deformed "wings" with ferrofluid, while a low-friction air interface further decreased the contact area

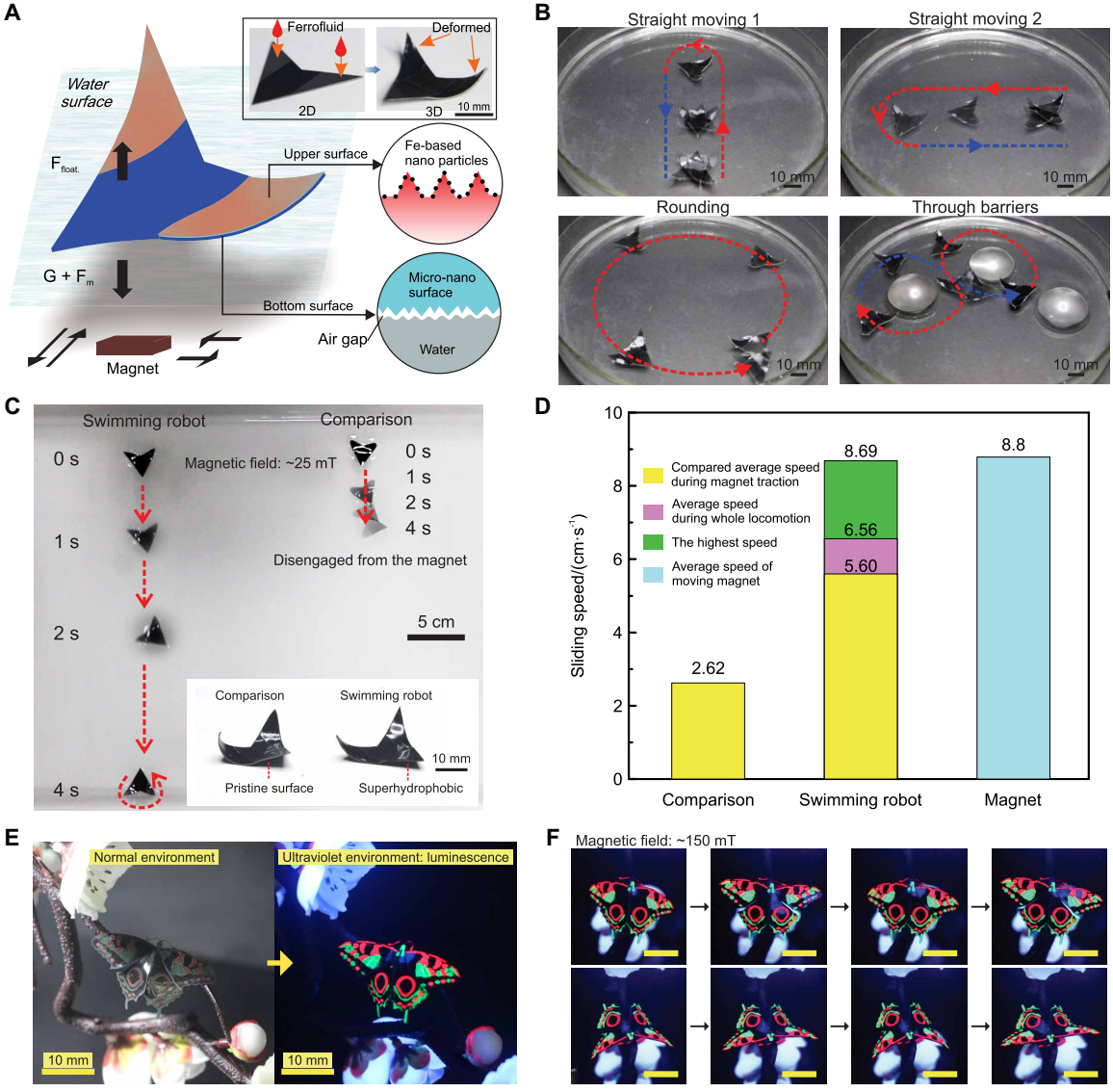

Fig. 4. Demonstrations of soft robots with multifunctionalized surfaces. (**A**) A low-friction swimming robot with magnetic actuating and superhydrophobic functional surfaces. (**B**) The swimming robot actuated with a magnet on a water surface. (**C** and **D**) Sliding comparison of swimming robot and counterpart with a pristine surface (C) and the quantified sliding speed (D). (**E** and **F**) Soft butterfly robots with luminescence warning coloration in a UV environment. Scale bars, 10 mm.

of the bottom layer with the water. Under the action of a magnet, the untethered swimming robot slid rapidly on the water surface (Fig. 4B, fig. S18, C and D, and movie S5). We also compared the sliding speed of a robot with a low-friction surface with that of a robot with a pristine surface (fig. S18E). As shown in movie S4 and Fig. 4 (C and D), the swimming robot exhibits a more agile spinning than the controlled group with a pristine surface. Initially, under the force provided by the magnet (~25 mT), these robots slide forward with average speeds of ~5.60 and ~2.62 cm/s, respectively. However, the reference robot with the pristine surface slows down because of the frictional resistance of the water. Over the course of the test, the swimming robot exhibits an average speed of ~6.56 cm/s, with a maximum speed of ~8.69 cm/s, when the magnet is moved at a speed of ~8.8 cm/s. In addition, by deploying a QD solution and ferrofluid spatially on different laser-scanned surfaces, we fabricated a butterfly-like robot with luminescence modules (Fig. 4E; design details are shown in fig. S19). Under visible light, the butterfly-like robot does not fluoresce, whereas under UV irradiation, a bright pattern of QD emission is observed. Soft robots with this design feature could be used to sense the presence of UV irradiation (Fig. 4F and movie S6).

A multimode locomotion robot was constructed by transforming a planar flower-like elastomer with several petals (Fig. 5A) into a soft robot with untethered soft ferromagnetic grippers (movie S7; geometry and fabrication details are shown in fig. S20A). The soft gripper can be manipulated using a permanent magnet (details in fig. S20B) to exhibit two modes of locomotion (Fig. 5B). In one mode, the robot moves by "somersaulting" (overturning); in the other mode, the robot advances by first standing sideways and then gathering its claws and rolling (rotation) (movie S7). The process discussed earlier for producing soft robots leads to a gradient in stiffness, with the highest stiffness at the iron oxide layer and the lowest stiffness in the soft elastomer interior (Fig. 5C), which is operative in each bent "claw." As a result, during delivery of a cargo, the soft robot can grasp the cargo with its claws (Fig. 5C) and move it to the destination (Fig. 5, D and E) while maintaining good adaptability in general. As shown in Fig. 5D and movie S7, the bent claw grasps a small pill and then moves to a destination; as shown in

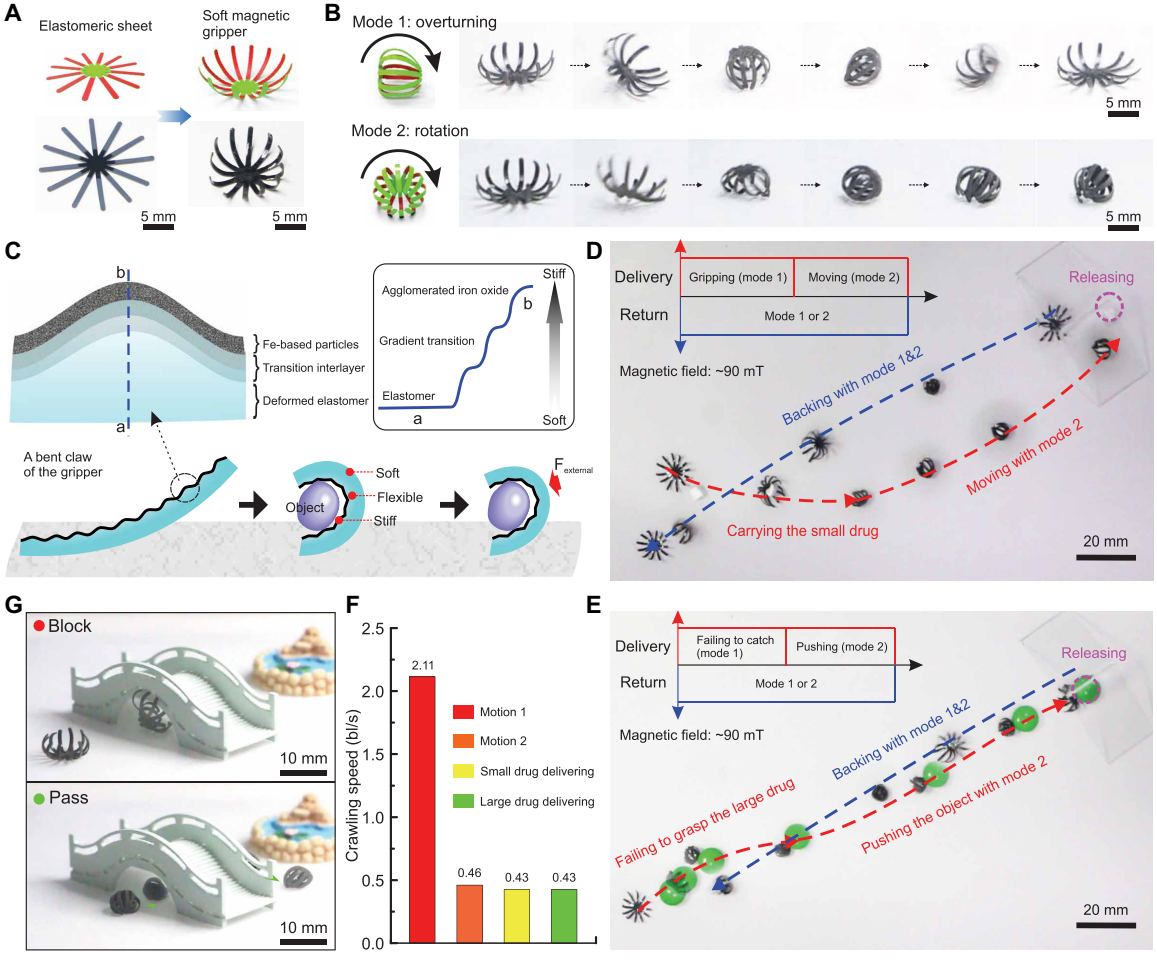

Fig. 5. Multilocomotion untethered soft carrier. (**A**) Schematic and experimental demonstration of configuring sample. (**B**) Illustration of two types of motion modes: overturning and rotation. (**C**) Schematic illustration of the soft-flexible-stiff structure for carrying and protecting an object when affected by an external force. (**D** and **E**) Demonstration of the soft carrier delivering pills of different sizes. (**F**) Calculated movement speeds of different motions and object deliveries. (**G**) Learning and adaptability when soft carrier passes through a restricting hole.

Fig. 5E, the claw fails to grasp a large pill and must push it to the destination. The crawling speed of overturning (~2.11 bl/s, where bl is body length) is greater than that of rotation (~0.46 bl/s) and drug delivery (~0.43 bl/s), because of a restriction on the magnet operation in the rotation mode (Fig. 5F). Figure 5G shows that the soft gripper can also sense external environments and can change its locomotion mode and size to pass under the bridge of a given height.

To further demonstrate the potential application of the multifunctional soft origami robot, and inspired by the chameleon, we fabricated a frog-like robot with switchable coloration to sense and respond to thermal and optical environmental stimuli (design and fabrication parameters are shown in fig. S21, A and B). As illustrated in Fig. 6 (A and B) and fig. S21C, a laser-scanned cPDMS sheet provides localized areas for selectively absorbing and pinning active coloration solutions—including thermochromic ink, photosensitive ink, QDs, and ferrofluid—onto the surface. This elastomeric sheet was configured into a multifunctional frog-like soft robot that could respond to external thermal and optical stimuli. On the basis of the switchable coloration shown in Fig. 6B, the behavior of this frog-like soft robot in a changing thermal and optical environment is shown in Fig. 6C and movie S8. At night (darkness, $T < 23$°C), the robot is nearly invisible because of the dark color of the cPDMS structure. When irradiated under a UV light, the QD luminescence modules are activated and result in a mimicry-trapping coloration. After sunrise (simulated by a sunlight simulator, T of ~30°C), the pattern turns into a warning coloration of bright red and yellow because of the direct exposure to strong sunlight. If the robot is continuously heated, the coloration turns into white, warning of an overheated environment. Subsequently, the robot jumps into the water to cool down (operational illustration is shown in fig. S21D), and the coloration is restored. This demonstration indicates that our approach can endow soft robots with biomimetic feedback and striking visual features based on skin color change.

DISCUSSION

By selectively tuning surface morphology using laser ablation, followed by treatment with solvent-containing active particles, we developed a facile, flexible approach to fabricate 3D ferromagnetic origami robots from planar elastomeric sheets. These sheets simultaneously and seamlessly integrated multiple functions: actuation, sensing, and visually striking modules. By adjusting the laser's operational parameters and the material's thickness, various deformed configurations can be produced and memorized by heterogeneous swelling and agglomeration of a rigid layer of active particles, respectively. For soft magnetic robots, this programmed origami process achieves an integrated structure with active functional modules. Furthermore, memorized origami-like configuration can be erased with exposure to compatible solvents and reprocessed. Thus, this procedure enables the fabrication of soft robots with high adaptability and offers designers more strategies for robot development. The various demonstrations conducted in this study—including development of a low-friction swimming robot, a butterfly-like robot with luminous color warning, an untethered soft carrier with adaptive locomotion, and a frog-like robot with switchable coloration—suggest that our fabrication strategy could be applied to various multifunctional soft systems.

At this juncture, several improvements can be envisioned to circumvent current limitations and provide additional functionality. First, the ferrofluid used is based on nonmagnetic polarity ferrous oxides. This restricts the degree of anisotropy in response to magnetic force and consequently restricts the diversity of actuating modes, as described in (*16*, *23*). Fortunately, we can achieve multimotion modes by taking advantage of stiffness-gradient structures in hybridized stiff iron oxides and soft elastomer. Nevertheless, if magnetic pole microparticles, e.g., NdFeB, can be combined in an ideal manner, then better control of the locomotion of origami robots may be achievable. Second, some functional particles on the rough

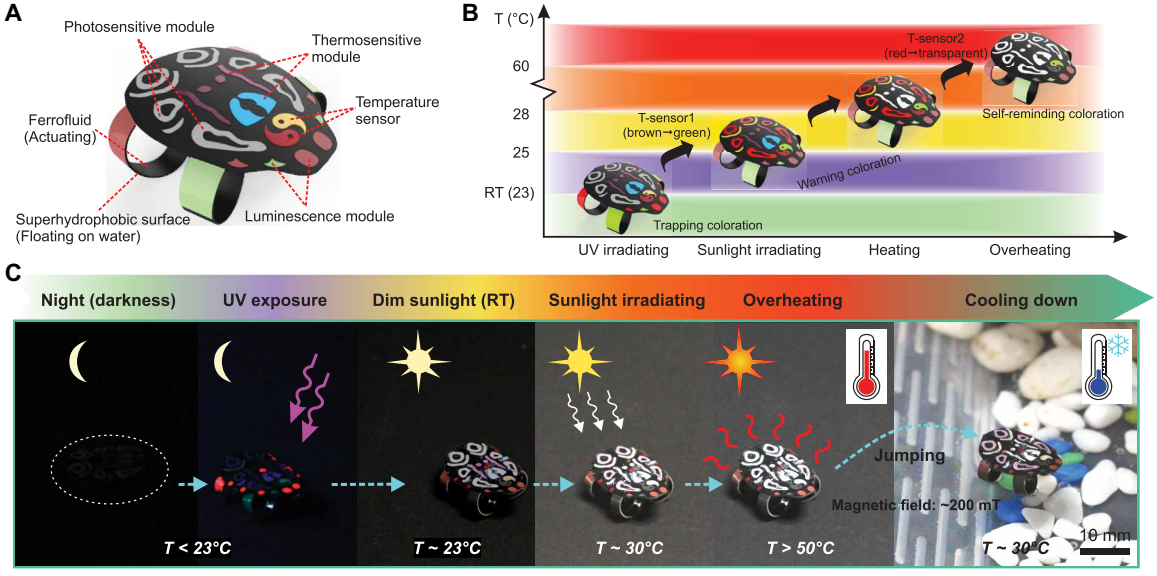

Fig. 6. A frog-like multifunctional robot with switchable coloration for active affecting and response with overheating/cooling feedback. (**A**) Schematic illustration of the configured frog-like robot with thermal, optical, and water-repelling modules. (**B**) Trigger design (temperature and light fields) for tripping, normal, warning, and self-reminding coloration switching. (**C**) Demonstration of the frog-like robot adapting to different circumstances with switchable coloration.

surface are not as mechanically resilient as ferrous oxides. For instance, fragmentary coloration patterns may occur as a result of non-optimized ink formulation and thickness control. Currently, an ultrathin layer of transparent PDMS encapsulates the robot at the expense of sacrificing reprocessability. Alternatively, thermochromic inks can be replaced with phosphor and fluorescence dyes. Third, the current configuration strategy works well for thin elastomeric sheets (<750 μm), but it is not as effective for thicker ones. Our strategy for thicker sheets may be improved by more powerful and more precise laser equipment. Last, if the strategy is used with smart composites or with other particle/compound/mixed-solvent solutions, it may be able to produce soft origami robots with various passive or active function modules.

MATERIALS AND METHODS

2D elastomeric sheet preparation

Carbon black (XC72R, Cabot, purchased from Alibaba, China) and a silicone base of PDMS (Sylgard 184, Dow Corning Corporation) were mixed manually with a glass rod for 3 min and then by digital stirring (RW 20, IKA, Germany) at ~2000 rpm for 2 to 3 min. After being cooled in a freezer for ~5 min, the mixture was then stirred with the curing agent for 3 min using a glass rod. The silicone base:curing agent:carbon black weight ratio was 10:1:0.1. After being vacuumed to remove bubbles, the mixture was spread on a thin flat aluminum plate (thickness of ~1 mm, purchased from Alibaba, China) with film applicators (PA2041, BYK, Wesel, Germany). Last, the cPDMS sheet was cured at 75°C for ~45 min in an oven (UF 55 plus, Memmert, Germany). The weights of the silicone base, curing agent, and carbon black were measured using an electronic balance (TP-A500, Huazhi Corporation, China). The 2D patterns used were designed in AutoCAD 2016 and imported into the laser operational program, EzCAD 2.12.4, where a series of parameters—such as the distance between adjacent scanning routes (ΔL), the orientation of the laser scanning routes (α), the scanning speed (v), the pulse repetition frequency (f), the pulse width (Q), and ablated areas—could be set for programming the surface morphology. The cured elastomeric sheets were selectively surface-modified using a UV laser marker (HGL-LSU3/5EI, Huagong Laser, Wuhan, China) with a pulse width (Q) of 0.10 μs and a working current of 33.5 A. The final pattern was cut using the same laser with a scanning speed (v) of 50 mm/s and a pulse width (Q) of 0.20 μs for processing 10 times. After the cutting, the residual material was removed with a tweezer, and the remaining elastomeric sheet was cleaned by spraying with IPA (Shenshi Chemical Industry Corporation, Wuhan, China) and was air-dried.

Configuring and reprocessing procedure

For the configuring process, ferrofluid purchased from Alibaba, China, composed of iron oxide particles (scale of <10 nm), a surfactant, and a solvent carrier (a mixture of hydrocarbons from n-decane to tetradecane), was dripped on a patterned 2D elastomeric sheet with a pipette (20 μl, Eppendorf, Hamburg, Germany). For comparison, the pure solvent carrier was dripped on a laser-ablated sample. For the reprocessing process, the configured samples with immobilized shapes were immersed into an IPA ultrasonic bath (40 kHz, 150 W, KQ3200DV, Kunshan Ultrasonic Instrument, Jiangsu, China), if necessary. After the agglomerated iron oxide–based nanoparticles on the surface were wiped away, the samples were allowed to air-dry until they were ready for reprocessing via laser ablation and other functional solvents. The pattern designs, processing parameters, and geometries of the samples are shown in figs. S6, S11, S14, S18A, S19, and S20A and table S1.

To visualize the diffusion process of ferrofluid penetrating into the PDMS matrix, a thick cPDMS-PDMS elastomeric composite was fabricated (fig. S4A) by hybridizing a surface layer of cPDMS (~100 μm) and a bulk layer of transparent PDMS (~700 μm). The PDMS layer was spread using a film applicator and semi-cured at 75°C for 10 min, after which the cPDMS layer was spread. The elastomeric composite was fully cured at 90°C for 45 min and then laser-treated eight times with parameter settings of v = 50 mm/s, ΔL = 0.1 mm, and Q = 0.20 μs. A mixture of 0.05 g of diesel colorant (blue, purchased from Taobao, Alibaba China) and 7.0 g of ferrofluid was mixed ultrasonically for 5 min. A 2.0-μl sample of this ferrofluid-colorant mixture was dripped onto the laser-scanned surface of the cPDMS-PDMS composite. The swelling and diffusion of the ferrofluid were recorded using a digital camera (EOS 70D, Canon, Tokyo, Japan) (Fig. 2A and fig. S4B). For the erasure process (Fig. 3A and fig. S12), the states of samples immersed in IPA were captured using an optical microscope (SMZ-161, Motic, China) equipped with a charge-coupled device (CCD) camera (Moticam 3+, Motic, China). Details of the experimental settings for shape contrast and the cyclic configuration-erasure process of "additive," "subtractive," and "subsurface" reprocessing are provided in text S3 and tables S2 and S3.

For electrical sensing module integration, about 50 μl of a AgNW/ethanol solution (AgNWs-30, average length of 20 μm and average diameter of 30 nm; 10 mg/ml; XFNano Materials Tech Co. Ltd., Nanjing, China) was dripped onto a laser-scanned area to form an electrical layer. The variable resistance was recorded using a multimeter (34461A, Keysight Technology, USA).

For the QD solution configuration, a 10-μl green QD solution (CsPbBr3/n-hexane) was dripped onto the surface of a laser-scanned cPDMS elastomer sheet using a pipette (fig. S17). The operational parameters of the laser used to scan the cPDMS elastomer sample were set to v = 100 mm/s and ΔL = 0.05 mm. The sample was cut into the shape shown in fig. S2C. The bending angles were measured from photographs captured by the CCD camera in the drop shape analysis equipment. Microviews and the elemental distribution were observed using an EPMA (EPMA-8050G, Shimadzu, Kyoto, Japan).

Design and fabrication of soft robot demonstrations

For the low-friction swimming robot, a 500-μm-thick cPDMS elastomer sheet was selectively patterned on both surfaces with laser parameters of v = 200 mm/s and ΔL = 0.05 mm. The laser-ablated areas of the upper surface were swollen and deformed into wings using ~5 μl of ferrofluid. A sample prepared for comparison was ablated only on the upper surface. The sliding competition was conducted in a plastic tank containing water ~2 cm deep. The NdFeB magnet used for actuation was purchased from Taobao (Alibaba, China) and had length, width, and thickness dimensions of 40 mm by 40 mm by 5 mm, respectively. For the butterfly-like robot, red (CdZnSe/ZnS/methylbenzene) and green ($CsPbBr_3$/n-hexane) QD solutions (purchased from Nading Optoelectronics Co. Ltd., Jiaxing, China) were used for surface doping as photoluminescence modules via a pipette (20 μl, Eppendorf, Hamburg, Germany), after the cPDMS sheet was configured by the ferrofluid. A UV lamp (wavelengths of 254 and 355 nm, purchased from Taobao, China) was used to illuminate the QDs. For the untethered soft gripper, a

500-μm-thick flower-like elastomeric sheet was configured into a claw-like gripper with ferrofluid and an average claw bending angle of ~120°. The masses of delivered drugs were ~0.2 and ~0.5 g, respectively. The delivery process, conducted on a 3-mm-thick polyethylene terephthalate plate, and the experiment of passing through a hole in a bridge were conducted using a NdFeB magnet with a size of 10 mm by 10 mm by 10 mm. For the frog-like robot, a 750-μm-thick cPDMS sheet was selectively ablated two to three times and configured with ferrofluid on the bottom surface. QDs were used for the patterning trapping coloration on the "legs" and "eyes." Thermochromic and photosensitive inks purchased from Taobao were dispersed into *N*-methyl pyrrolidone (NMP) (Aladdin Bio-Chem Technology Co. Ltd., Shanghai, China) via 5 min of ultrasonic stirring to form a suspension (0.5 g/ml). The normal, warning, and self-reminding colorations were patterned with an ink-NMP suspension using a pipette. Sunlight was simulated using a white light source (SOLA AM 5-LCR-VA, Lumencor, USA). A heating field was simulated using a hot plate (AZ2015, Anzhuo Co. Ltd., Shenzhen, China), and the real-time temperature was monitored using a Bluetooth temperature sensor (purchased from the Xiaomi online shop).

Characterizations

The contact angles of ferrofluid droplets on pristine and laser-treated cPDMS surfaces were measured using drop shape analysis equipment (DSA25, Kruss, Germany) and the sessile drop method. A ferrofluid droplet was dripped with a syringe pump (PUMP 11 ELITE Nanomite, Harvard Apparatus, Holliston, MA) to precisely control the volume. The process of deforming the sample was recorded with the video acquisition module of the drop shape analysis equipment. On the basis of the captured digital images during the swelling and deformation process, variable bending angles and twist angles were measured using the ImageJ software, and curvatures were fitted using a program coded in MATLAB (version R2018a, MathWorks, Natic, MA). The surface morphologies of the pristine and laser-treated samples were examined using a field scanning electron microscope (GeminiSEM 300, Carl Zeiss, Germany). The elemental distribution of the surface was measured with an EPMA (EPMA-8050G). The surface roughness was measured and calculated using an ultradepth 3D microscope (DSX510, Olympus, Japan). To calculate the speeds of movement of the swimming robot and untethered soft grippers, the following assumptions were made: Movement fluctuation was neglected, and the locomotion of the soft magnetic grippers was regarded as linear movement. We recorded the locomotion distances (Ld) and times (T) and calibrated the diameter of the magnetic grippers during locomotion in terms of its body length (Lb). We calculated the kinematic velocity (V) for different movement modes and drug delivery tasks as $V = Ld / (Lb \times T)$. Photographs and videos of the movement were recorded using the digital camera.

SUPPLEMENTARY MATERIALS

robotics.sciencemag.org/cgi/content/full/6/53/eabd6107/DC1

Text

Fig. S1. Light absorption, surface topography, and deformability comparison of cPDMS, black-PDMS, Fe-PDMS, and PDMS.

Fig. S2. Microviews, characterization, and schematic illustration of swelling elastomer sample.

Fig. S3. The behavior of ferrofluid droplet on pristine and laser-scanned cPDMS surface.

Fig. S4. Visualization investigation of diesel colorant–mixed ferrofluid penetrating and diffusing into silicone matrix.

Fig. S5. Swelling and deforming process with pure solvent carrier.

Fig. S6. Elemental analysis of cross profile of the configured elastomeric ribbon sample.

Fig. S7. Influence of carbon content and used volume of ferrofluid.

Fig. S8. The relation of twisting curvature with the thickness (t) and adjacent distance (ΔL).

Fig. S9. Characterization of the swelling and deforming process.

Fig. S10. Demonstrations of configured origami robots based on programmable elastomeric sheets.

Fig. S11. Designed geometry of programmable 2D elastomeric sheet for configuring 3D soft origami robots demonstrated in Fig. 2.

Fig. S12. Visualization investigation of erasure process of IPA solvent penetrating and diffusing into silicone matrix.

Fig. S13. Detailed mechanism and characterization of recovering process.

Fig. S14. Designed geometry and processing laser parameters for reprocessable demonstration in Fig. 3.

Fig. S15. Characterization of recovering process.

Fig. S16. Shape contrast and reusage test of additive, subtractive, and subsurface reprocessing.

Fig. S17. Characterization of QD swelling process.

Fig. S18. Design and test of the low-friction swimming robot.

Fig. S19. Schematic illustration and experimental demonstration of the soft butterfly-like robot.

Fig. S20. Design of the untethered soft gripper and the controlling operation via a magnet.

Fig. S21. Fabrication and actuating details of the frog-like robot.

Table S1. Fabrication parameter setting of programming 2D elastomeric sheets for configuring 3D origami robots in Fig. 2.

Table S2. Fabrication parameter settings for shape contrast of additive, subtractive, and subsurface reprocessing.

Table S3. Fabrication parameter settings for recycling test of additive, subtractive, and subsurface reprocessing.

Movie S1 (.mp4 format). Configuring and recovering process.

Movie S2 (.mp4 format). Visualization of diffusion process.

Movie S3 (.mp4 format). Actuation and recovering of origami robots.

Movie S4 (.mp4 format). Locomotion mode reconfiguration.

Movie S5 (.mp4 format). The low-friction swimming robot.

Movie S6 (.mp4 format). The soft butterfly-like robot.

Movie S7 (.mp4 format). Multilocomotion soft gripper.

Movie S8 (.mp4 format). Frog-like multifunctional robot.

REFERENCES AND NOTES

1. D. Rus, M. T. Tolley, Design, fabrication and control of soft robots. *Nature* **521**, 467–475 (2015).
2. G.-Z. Yang, J. Bellingham, P. E. Dupont, P. Fischer, L. Floridi, R. Full, N. Jacobstein, V. Kumar, M. McNutt, R. Merrifield, B. J. Nelson, B. Scassellati, M. Taddeo, R. Taylor, M. Veloso, Z. L. Wang, R. Wood, The grand challenges of *Science Robotics*. *Sci. Robot.* **3**, eaar7650 (2018).
3. C. Majidi, Soft robotics: A perspective—Current trends and prospects for the future. *Soft Robot.* **1**, 5–11 (2014).
4. Y. Yu, J. Nassar, C. Xu, J. Min, Y. Yang, A. Dai, R. Doshi, A. Huang, Y. Song, R. Gehlha, A. D. Ames, W. Gao, Biofuel-powered soft electronic skin with multiplexed and wireless sensing for human-machine interfaces. *Sci. Robot.* **5**, eaaz7946 (2020).
5. S.-M. Baek, S. Yim, S.-H. Chae, D.-Y. Lee, K.-J. Cho, Ladybird beetle–inspired compliant origami. *Sci. Robot.* **5**, eaaz6262 (2020).
6. S. Kim, C. Laschi, B. Trimmer, Soft robotics: A bioinspired evolution in robotics. *Trends Biotechnol.* **31**, 287–294 (2013).
7. Y. Wang, X. Yang, Y. Chen, D. K. Wainwright, C. P. Kenaley, Z. Gong, Z. Liu, H. Liu, J. Guan, T. Wang, J. C. Weaver, R. J. Wood, L. Wen, A biorobotic adhesive disc for underwater hitchhiking inspired by the remora suckerfish. *Sci. Robot.* **2**, eaan8072 (2017).
8. M. Sitti, Miniature soft robots—Road to the clinic. *Nat. Rev. Mater.* **3**, 74–75 (2018).
9. M. Cianchetti, C. Laschi, A. Menciassi, P. Dario, Biomedical applications of soft robotics. *Nat. Rev. Mater.* **3**, 143–153 (2018).
10. M. Cianchetti, T. Ranzani, G. Gerboni, T. Nanayakkara, K. Althoefer, P. Dasgupta, A. Menciassi, Soft robotics technologies to address shortcomings in today's minimally invasive surgery: The STIFF-FLOP approach. *Soft Robot.* **1**, 122–131 (2014).
11. E. W. Hawkes, L. H. Blumenschein, J. D. Greer, A. M. Okamura, A soft robot that navigates its environment through growth. *Sci. Robot.* **2**, eaan3028 (2017).
12. L. Yang, L. Chang, Y. Hu, M. Huang, Q. Ji, P. Lu, J. Liu, W. Chen, Y. Wu, An autonomous soft actuator with light-driven self-sustained wavelike oscillation for phototactic self-locomotion and power generation. *Adv. Funct. Mater.* **30**, 1908842 (2020).
13. M. Wehner, R. L. Truby, D. J. Fitzgerald, B. Mosadegh, G. M. Whitesides, J. A. Lewis, R. J. Wood, An integrated design and fabrication strategy for entirely soft, autonomous robots. *Nature* **536**, 451–455 (2016).
14. C. Wang, K. Sim, J. Chen, H. Kim, Z. Rao, Y. Li, W. Chen, J. Song, R. Verduzco, C. Yu, Soft ultrathin electronics innervated adaptive fully soft robots. *Adv. Mater.* **30**, 1706695 (2018).

15. K. B. Justus, T. Hellebrekers, D. D. Lewis, A. Wood, C. Ingham, C. Majidi, P. R. LeDuc, C. Tan, A biosensing soft robot: Autonomous parsing of chemical signals through integrated organic and inorganic interfaces. *Sci. Robot.* **4**, eaax0765 (2019).
16. W. Hu, G. Z. Lum, M. Mastrangeli, M. Sitti, Small-scale soft-bodied robot with multimodal locomotion. *Nature* **554**, 81–85 (2018).
17. J. Z. Gul, M. Sajid, M. M. Rehman, G. U. Siddiqui, I. Shah, K.-H. Kim, J.-W. Lee, K. H. Choi, 3D printing for soft robotics - a review. *Sci. Technol. Adv. Mater.* **19**, 243–262 (2018).
18. T. J. Wallin, J. Pikul, R. F. Shepherd, 3D printing of soft robotic systems. *Nat. Rev. Mater.* **3**, 84–100 (2018).
19. A. S. Gladman, E. A. Matsumoto, R. G. Nuzzo, L. Mahadevan, J. A. Lewis, Biomimetic 4D printing. *Nat. Mater.* **15**, 413–418 (2016).
20. Z. Zhang, K. G. Demir, G. X. Gu, Developments in 4D-printing: A review on current smart materials, technologies, and applications. *Int. J. Smart Nano Mater.* **10**, 205–224 (2019).
21. J. Choi, O. C. Kwon, W. Jo, H. J. Lee, M.-W. Moon, 4D printing technology: A review. *3D Print. Addit. Manuf.* **2**, 159–167 (2015).
22. N. W. Bartlett, M. T. Tolley, J. T. B. Overvelde, J. C. Weaver, B. Mosadegh, K. Bertoldi, G. M. Whitesides, R. J. Wood, A 3D-printed, functionally graded soft robot powered by combustion. *Science* **349**, 161–165 (2015).
23. Y. Kim, H. Yuk, R. Zhao, S. A. Chester, X. Zhao, Printing ferromagnetic domains for untethered fast-transforming soft materials. *Nature* **558**, 274–279 (2018).
24. M. L. Hammock, A. Chortos, C.-K. Tee, J. B.-H. Tok, Z. Bao, 25th anniversary article: The evolution of electronic skin (e-skin): A brief history, design considerations, and recent progress. *Adv. Mater.* **25**, 5997–6038 (2013).
25. S. Gong, D. T. H. Lai, B. Su, K. J. Si, Z. Ma, L. W. Yap, P. Guo, W. Cheng, Highly stretchy black gold E-skin nanopatches as highly sensitive wearable biomedical sensors. *Adv. Electron. Mater.* **1**, 1400063 (2015).
26. J. C. Yang, J. Mun, S. Y. Kwon, S. Park, Z. Bao, S. Park, Electronic skin: Recent progress and future prospects for skin-attachable devices for health monitoring, robotics, and prosthetics. *Adv. Mater.* **31**, e1904765 (2019).
27. J. W. Booth, D. Shah, J. C. Case, E. L. White, M. C. Yuen, O. Cyr-Choiniere, R. Kramer-Bottiglio, OmniSkins: Robotic skins that turn inanimate objects into multifunctional robots. *Sci. Robot.* **3**, eaat1853 (2018).
28. J. Byun, Y. Lee, J. Yoon, B. Lee, E. Oh, S. Chung, T. Lee, K.-J. Cho, J. Kim, Y. Hong, Electronic skins for soft, compact, reversible assembly of wirelessly activated fully soft robots. *Sci. Robot.* **3**, eaas9020 (2018).
29. S. Zhang, B. Wang, J. Jiang, K. Wu, C. F. Guo, Z. Wu, High-fidelity conformal printing of 3D liquid alloy circuits for soft electronics. *ACS Appl Mater & Interfaces* **11**, 7148–7156 (2019).
30. C. M. Boutry, M. Negre, M. Jorda, O. Vardoulis, A. Chortos, O. Khatib, Z. Bao, A hierarchically patterned, bioinspired e-skin able to detect the direction of applied pressure for robotics. *Sci. Robot.* **3**, eaau6914 (2018).
31. Y.-C. Lai, J. Deng, R. Liu, Y.-C. Hsiao, S. L. Zhang, W. Peng, H.-M. Wu, X. Wang, Z. L. Wang, Actively perceiving and responsive soft robots enabled by self-powered, highly extensible, and highly sensitive triboelectric proximity- and pressure-sensing skins. *Adv. Mater.* **30**, e1801114 (2018).
32. H. Lipson, Challenges and opportunities for design, simulation, and fabrication of soft robots. *Soft Robot.* **1**, 21–27 (2014).
33. C. Lee, M. Kim, Y. J. Kim, N. Hong, S. Ryu, H. J. Kim, S. Kim, Soft robot review. *Int. J. Control Autom. Syst.* **15**, 3–15 (2017).
34. S. Cheng, Y. S. Narang, C. Yang, Z. Suo, R. D. Howe, Stick-on large-strain sensors for soft robots. *Adv. Mater. Interfaces* **6**, 1900985 (2019).
35. C. Larson, B. Peele, S. Li, S. Robinson, M. Totaro, L. Beccai, B. Mazzolai, R. Shepherd, Highly stretchable electroluminescent skin for optical signaling and tactile sensing. *Science* **351**, 1071–1074 (2016).
36. D. Rus, M. T. Tolley, Design, fabrication and control of origami robots. *Nat. Rev. Mater.* **3**, 101–112 (2018).
37. Q. Ge, C. K. Dunn, H. J. Qi, M. L. Dunn, Active origami by 4D printing. *Smart Mater. Struct.* **23**, 094007 (2014).
38. X. Zheng, J. Deotte, M. P. Alonso, G. R. Farquar, T. H. Weisgraber, S. Gemberling, H. Lee, N. Fang, C. M. Spadaccini, Design and optimization of a light-emitting diode projection micro-stereolithography three-dimensional manufacturing system. *Rev. Sci. Instrum.* **83**, 125001 (2012).
39. N. T. Jafferis, E. F. Helbling, M. Karpelson, R. J. Wood, Untethered flight of an insect-sized flapping-wing microscale aerial vehicle. *Nature* **570**, 491–495 (2019).
40. Y. Chen, H. Zhao, J. Mao, P. Chirarattananon, E. F. Helbling, N.-s. P. Hyun, D. R. Clarke, R. J. Wood, Controlled flight of a microrobot powered by soft artificial muscles. *Nature* **575**, 324–329 (2019).
41. K.-U. Jeong, J.-H. Jang, D.-Y. Kim, C. Nah, J. H. Lee, M.-H. Lee, H.-J. Sun, C.-L. Wang, S. Z. D. Cheng, E. L. Thomas, Three-dimensional actuators transformed from the programmed two-dimensional structures *via* bending, twisting and folding mechanisms. *J. Mater. Chem.* **21**, 6824–6830 (2011).
42. J. N. Lee, C. Park, G. M. Whitesides, Solvent compatibility of poly(dimethylsiloxane)-based microfluidic devices. *Anal. Chem.* **75**, 6544–6554 (2003).
43. R. Mukhopadhyay, When PDMS isn't the best. *Anal. Chem.* **79**, 3248–3253 (2007).

Acknowledgments: We thank J. Jiang for helping draw Fig. 1 and B. Zhou for supplying the QD solutions. **Funding:** This work was partly financially supported by the National Natural Science Foundation of China (U1613204 and L1924046) and by the National Key R&D program of China (2017YFB1303100). **Author contributions:** S.Z., H.D., and Z.W. conceived and designed the study. S.Z. performed the design, fabrication, and demonstration and conducted the experiments with the assistance of X.K. and Q.J. All authors contributed to the discussion. S.Z. and Z.W. wrote the manuscript, with input from all authors. Z.W. and H.D. supervised and supported the study. **Competing interests:** The authors declare that they have no competing financial interests. **Data and materials availability:** All data needed to evaluate the conclusions presented in the paper are provided in the paper or the Supplementary Materials.

Submitted 1 July 2020
Accepted 15 March 2021
Published 7 April 2021
10.1126/scirobotics.abd6107

Citation: S. Zhang, X. Ke, Q. Jiang, H. Ding, Z. Wu, Programmable and reprocessable multifunctional elastomeric sheets for soft origami robots. *Sci. Robot.* **6**, eabd6107 (2021).

Science Robotics

Programmable and reprocessable multifunctional elastomeric sheets for soft origami robots

Shuo Zhang, Xingxing Ke, Qin Jiang, Han Ding, and Zhigang Wu

Sci. Robot. **6** (53), eabd6107. DOI: 10.1126/scirobotics.abd6107

Science Robotics (ISSN 2470-9476) is published by the American Association for the Advancement of Science. 1200 New York Avenue NW, Washington, DC 20005. The title *Science Robotics* is a registered trademark of AAAS.